



1 **Enhancing GNSS Water Vapor Retrieval via Synergistic Microwave** 2 **Radiometry: Thermodynamic Error Diagnosis and Bias Correction**

3 Avinash N. Parde¹, Christina Oikonomou¹, Haris Haralambous^{1,2}

4 ¹Frederick Research Center, Nicosia, 1303, Republic of Cyprus

5 ²Frederick University, Nicosia, 1036, Republic of Cyprus

6 **Correspondence:** Avinash N. Parde (aviparde07@gmail.com)

7

8 **Abstract.**

9 The retrieval of Precipitable Water Vapor (PWV) from Global Navigation Satellite Systems (GNSS) in thermodynamically
10 complex environments is fundamentally limited by the accuracy of the weighted mean temperature (T_m). This study evaluates
11 the efficacy of static climatological models versus dynamic ground-based microwave radiometry for T_m determination in the
12 Eastern Mediterranean, a region characterized by sharp refractivity gradients. Using the Cyprus GNSS Meteorology
13 Enhancement (CYGMEN) infrastructure in Nicosia, the performance of the ERA5-based HGPT2 model and a co-located
14 Microwave Radiometer (MWR) was assessed against radiosonde (RS) profiles during the 2025 warm season (Spring–
15 Summer). Diagnostic analysis reveals that the static HGPT2 model fails to resolve the diurnal thermodynamic decoupling
16 between the boundary layer and the free troposphere, leading to a systematic overestimation of T_m exceeding 6 K during peak
17 solar insolation. Conversely, the MWR captures short-term thermodynamic variability ($r=0.98$) but exhibits a systematic cold
18 bias of -1.91 K in raw retrievals. It is demonstrated that a site-specific linear bias correction reduces the MWR T_m Root Mean
19 Square Error (RMSE) from 2.32 K to 1.43 K, significantly outperforming the empirical model. Sensitivity analysis confirms
20 that thermodynamic uncertainty dominates the error budget, outweighing uncertainties in refractivity constants by an order of
21 magnitude. Consequently, standard climatological retrievals diverge from the synergistic MWR-GNSS method during extreme
22 hygrometric events, introducing systematic PWV biases exceeding 1.0 mm when moisture levels surpass 45 mm. The
23 synergistic coupling of real-time radiometric T_m with GNSS data is therefore essential for generating climate-quality PWV
24 records in semi-arid coastal regions.

25

26 **1 Introduction**

27 Atmospheric water vapor (WV) is the primary greenhouse gas, contributing approximately 60% to the natural greenhouse
28 effect and playing a vital role in regulating the Earth's thermodynamic budget (Kiehl and Trenberth, 1997; Trenberth et al.,
29 2005). Furthermore, WV is the main driver of latent heat transport, influencing convective systems and global precipitation



30 patterns. High-frequency variations in Precipitable Water Vapor (PWV) correlate strongly with atmospheric instability and are
31 a key factor in the initiation of severe weather. Specifically, rapid temporal gradients in PWV often precede heavy rainfall and
32 flash floods, acting as a reliable precursor for convective storms (Brenot et al., 2013). Consequently, assimilating high-
33 resolution PWV data into Numerical Weather Prediction (NWP) models significantly improves short-range precipitation
34 "nowcasting" (Bennitt and Jupp, 2012). Accurate PWV retrieval is especially crucial for the Eastern Mediterranean (EM), a
35 climate change "hotspot" warming faster than the global average (Giorgi, 2006; Lelieveld et al., 2012). This region is
36 characterized by complex topography and land-sea contrasts, which create sharp atmospheric refractivity gradients. The EM
37 faces a hydro-climatic paradox: a long-term drying trend (-0.5 mm/decade) alongside increasing high-intensity, short-duration
38 flash flood events (Zittis et al., 2019; Ziv et al., 2021). GNSS-derived PWV in this region exhibits strong diurnal cycles with
39 amplitudes up to 5 mm, which are closely correlated with atmospheric instability (Ziskin Ziv et al., 2020). Despite this
40 vulnerability, the EM currently lacks dense, continuous atmospheric profiling networks. Traditional observation methods, such
41 as radiosondes (RS), fail to resolve these mesoscale events due to low temporal resolution (typically 12-hour intervals) and
42 significant spatial gaps (Soden and Lanzante, 1996). While satellite-based passive remote sensing offers global coverage, it is
43 often limited by revisit times, daylight dependence, or data degradation in coastal zones due to land contamination in the
44 microwave footprint (Bennartz and Bauer, 2003).

45 These limitations underscore the necessity for ground-based remote sensing techniques that offer continuous, all-weather
46 operability. Ground-based Global Navigation Satellite Systems (GNSS) meteorology has emerged as a robust technique for
47 atmospheric sounding since the seminal proposal by Bevis et al. (1992). By estimating the Zenith Total Delay (ZTD) of GNSS
48 signals traversing the neutral atmosphere, the Zenith Wet Delay (ZWD) can be isolated by subtracting the Zenith Hydrostatic
49 Delay (ZHD), which is accurately modeled from surface pressure observations (Saastamoinen, 1972). GNSS-derived PWV
50 offers significant advantages, including high temporal resolution (sub-hourly), all-weather availability, and cost-efficiency by
51 leveraging existing geodetic infrastructure (Guerova et al., 2016; Jones et al., 2020).

52 The retrieval of PWV from GNSS ZWD relies on a dimensionless conversion factor, Π , which is a function of the
53 atmospheric weighted mean temperature, T_m . Defined physically as $\int (e/T) dz / \int (e/T^2) dz$ (Askne and Nordius, 1987), T_m
54 encapsulates the thermal state of the atmospheric column. The accuracy of the derived PWV is linearly dependent on the
55 accuracy of T_m . Theoretical sensitivity analyses indicate that a 1 K error in T_m propagates to approximately 0.3–0.5 mm bias
56 in PWV, dominating the uncertainty budget ($>50\%$) at high PWV levels (>50 mm) in empirical models (Bevis et al., 1994;
57 Jiang et al., 2019). Therefore, the determination of T_m is the primary source of uncertainty in GNSS meteorology after ZTD
58 estimation. In the absence of in-situ profiles, T_m is commonly estimated using empirical regression models or global
59 climatological models. However, earlier studies have demonstrated that empirical T_m regressions, such as the Bevis model
60 (Bevis et al., 1992), introduce relative PWV errors of 1–2% (equivalent to 1–2 mm RMSE) due to weak T_s – T_m correlations in
61 coastal and equatorial regions, where annual/semiannual variations are not adequately captured (Yao et al., 2014; Lan et al.,



62 2016). Similarly, global grid-based T_m models like GPT2w achieve RMSE <4 K at $\sim 80\%$ of mid-latitude sites but degrade in
63 data-sparse areas like the Middle East and Africa, where reanalysis quality is limited (Böhm et al., 2015; Jiang et al., 2019).
64 The Hourly Global Pressure and Temperature 2 (HGPT2) model represents a major advancement by providing hourly estimates
65 derived from ERA5 reanalysis (Mateus et al., 2021). Despite recent validation of GPT2w and ECMWF models for Integrated
66 Water Vapor (IWV) retrieval in the Mediterranean (Oikonomou et al. 2018), a critical gap exists: the quantification of vertical
67 interpolation errors in these models, especially over complex coastal terrains. For instance, while recent validation studies in
68 Cyprus demonstrate strong GNSS-PWV correlations (>0.6) with ERA5 during extreme precipitation, persistent reanalysis
69 interpolation errors are highlighted in mountainous areas (Giannadaki et al., 2025). This lack of validation for HGPT2's
70 performance in the complex topography of the EM potentially exacerbates PWV biases during extreme events.

71 An alternative approach to deriving T_m is the use of ground-based Microwave Radiometers (MWR). MWRs measure
72 brightness temperatures at multiple frequencies to retrieve continuous vertical profiles of temperature and humidity. Ground-
73 based MWRs have been shown to retrieve T_m with RMSE $\sim 1\text{--}2$ K in mid-latitudes, outperforming empirical models during
74 synoptic anomalies (Cimini et al., 2010; Crewell and Löhnert, 2007; Löhnert et al., 2012). While multi-site intercomparisons
75 reveal that MWR retrievals can exhibit upper-tropospheric cold biases (up to 5 K at >2 km altitude) (Van Malderen et al.,
76 2014; Steinke et al., 2015), simple linear corrections can reduce RMSE by 20–40% (Ning and Elgered, 2021). Operational
77 GNSS–MWR synergies for T_m bias correction have documented gains in PWV accuracy (10–30% RMSE reduction) in
78 European networks (Vaquero-Martínez et al., 2018; Li et al., 2020). However, such applications are rare in the semi-arid EM,
79 where MWR could critically mitigate reanalysis uncertainties.

80 This study leverages the infrastructure of the CYGMEN (Cyprus GNSS Meteorology Enhancement) project, which is
81 establishing a dense, multi-sensor meteorological network in Cyprus. The network, termed CyMETEO, integrates continuous
82 GNSS stations with co-located MWR and RS launch sites. This unique instrumental setup provides an ideal testbed for inter-
83 comparing atmospheric retrieval techniques in a coastal, semi-arid environment. The primary objective of this manuscript is
84 to evaluate the accuracy of GNSS-derived PWV over the Eastern Mediterranean by assessing the performance of different T_m
85 determination strategies. We specifically investigate the efficacy of the HGPT2 model compared to MWR-derived T_m and RS
86 benchmarks. The study aims to quantify the error budget of GNSS-PWV and determine whether the inclusion of MWR data
87 provides statistically significant improvements over the state-of-the-art HGPT2 model. The manuscript is organized as follows:
88 Section 2 describes the study area and the instrumentation of the CYGMEN network; Section 3 details the methodology for
89 GNSS processing, ZTD estimation, and the mathematical derivation of T_m from different sources; Section 4 presents the
90 validation results and statistical analysis against RS reference data; and Section 5 concludes with recommendations for
91 operational PWV monitoring strategies in the region.

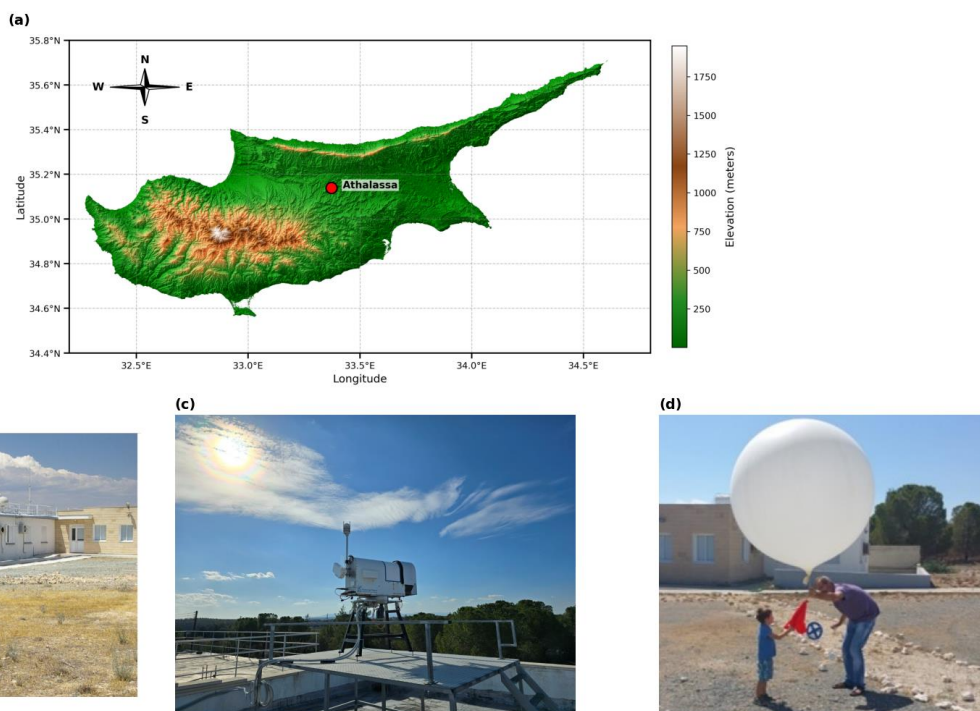
92



93 **2 Data and Methodology**

94 **2.1 Observational Site and CYGMEN Infrastructure**

95 The observational campaign was conducted at the Athalassa atmospheric observatory in Nicosia, Cyprus (35.15°N, 33.40°E,
 96 160 m a.s.l.), situated in the central Mesaoria plain. The site is characterized by complex topography, bounded by the Troodos
 97 Mountain to the southwest and the Pentadaktylos Mountain to the north, as shown in Fig. 1a. This study presents the first
 98 comprehensive analysis of radiometric data acquired under the Cyprus GNSS Meteorology Enhancement (CYGMEN)
 99 infrastructure project, established to monitor the thermodynamic state of the Eastern Mediterranean atmosphere. To ensure
 100 robust thermodynamic profiling and validation, three primary datasets were collated, as shown in Table 1:



101 **Figure 1.** Location and instrumentation at Athalassa, Cyprus. (a) Site location on the island's elevation map. (b) GNSS reference station.
 102
 103 (c) RPG-HATPRO radiometer. (d) Radiosonde balloon launching.

104 **Table 1:** Summary of Instrumentation and Datasets

Parameter	Microwave Radiometer (MWR)	Radiosonde (RS)	GNSS Station
Instrument Model	HATPRO-Gen5 (RPG)	Vaisala RS41-SGP	GNSS Receiver LEICA GR50 (Collocated)
Role in Study	Synergistic thermodynamic profiling (temperature and humidity)	<i>In-situ</i> "Ground Truth" Reference	ZTD Source for PWV Retrieval



Observation Type	Passive remote sensing (22–58 GHz)	<i>In-situ</i> vertical profile (balloon-borne)	Continuous satellite signal delay
Key Variables	Brightness Temp (T_B), $T(z)$, $\rho_v(z)$, IWV	$P(z)$, $T(z)$, $RH(z)$, Geopotential Height	Zenith Total Delay (ZTD)
Vertical Range	Surface to 10 km (94 levels)	Surface to burst altitude (~30 km)	Column-integrated (single value)
Temporal Resolution	High frequency (~1 sec raw, resampled to 15 min)	Periodic (launch dependent)	Continuous (high rate)
Accuracy / Noise	T_B noise < 0.11 K (K-band), < 0.32 K (V-band)	T : 0.3 K, RH : 4% (Manufacturer spec)	ZTD precision ~mm level
Auxiliary Data	Vaisala WXT536 (Rain, Surface Met)	GPS position/height	Surface Pressure

105

106 2.2 Instrumentation and Data Processing

107 2.2.1 Microwave Radiometry (MWR)

108 The RPG-HATPRO radiometer observes downwelling atmospheric brightness temperatures (T_B) across 14 channels: seven in
 109 the K-band (22–31 GHz) sensitive to water vapor, and seven in the V-band (51–58 GHz) sensitive to oxygen for temperature
 110 profiling. This instrument enables the continuous retrieval of temperature (T) and absolute humidity (ρ_v) profiles on a
 111 standardized grid of 94 vertical levels from the surface up to 10 km. The vertical resolution is optimized for the planetary
 112 boundary layer (PBL), ranging from 10–30 m up to 500 m, and decreasing to 100–500 m in the free troposphere. For this
 113 study, high-frequency MWR observations were resampled to 15-minute intervals to align with GNSS processing epochs. To
 114 diagnose potential biases in the MWR-derived T_m , the dataset was split into a Training Set (April–June 2025) for regression
 115 modeling and a Validation Set (July–October 2025) for independent testing.

116

117 2.2.2 Radiosonde Data Processing

118 To establish a rigorous validation dataset, Integrated Water Vapor (IWV) was derived from high-resolution vertical profiles
 119 obtained from collocated radiosonde launches. A strict collocation window was applied, where MWR profiles were averaged
 120 within ± 30 minutes of the balloon launch time. The raw telemetry data, comprising pressure (P), temperature, and dew point
 121 temperature (T_d), were processed to derive the total columnar water vapor content (in kg m^{-2}) through the vertical integration
 122 of specific humidity, assuming the atmosphere is in hydrostatic equilibrium. The determination of the necessary moisture



123 variables relied on the Magnus-Tetens approximation, which provides a widely accepted empirical relationship for saturation
124 vapor pressure. First, the actual vapor pressure (e , in hPa) was computed directly from the dew point temperature (T_d , in °C).
125 This calculation utilized the coefficients defined by Bolton (1980), which are optimized for saturation vapor pressure over
126 liquid water in the meteorological temperature range, as shown in Eq. (1):

$$127 \quad e = 6.112 \cdot \exp\left(\frac{17.67 \cdot T_d}{T_d + 243.5}\right) \quad (1)$$

128 Subsequently, the specific humidity (q , in kg kg⁻¹) was derived via Eq. (2), representing the mass mixing ratio of water vapor
129 to the total moist air parcel:

$$130 \quad q = \frac{\epsilon \cdot e}{P - (1 - \epsilon) \cdot e} \quad (2)$$

131 where P is the static pressure (hPa) and $\epsilon \approx 0.622$ represents the ratio of the molecular weight of water vapor to that of dry air.
132 Once the specific humidity profile was established, the total column IWV was calculated by integrating q with respect to
133 pressure. The retrieval algorithm employed the trapezoidal rule for numerical integration, which approximates the integral as
134 the sum of discrete atmospheric layers (Eq. 3):

$$135 \quad IWV = \frac{1}{g} \sum_{i=0}^{N-1} \frac{q_i + q_{i+1}}{2} \cdot |P_{i+1} - P_i| \quad (3)$$

136 where g is the gravity dependent on altitude, $g(\phi, h)$, where ϕ represents the Geodetic latitude and h is the orthometric height.
137 P is converted to Pascals (Pa) prior to integration and N represents the total number of vertical levels in the RS profile. To
138 ensure a rigorous, 'apples-to-apples' intercomparison with the active MWR, the radiosonde integration was strictly confined to
139 a maximum altitude of 10 km Above Ground Level (AGL). This vertical cutoff was deliberately chosen to exactly match the
140 10 km ceiling of the standard RPG-HATPRO retrieval grid. While GNSS integrates delays through the entire atmosphere,
141 bounding the in-situ reference data is mathematically necessary to isolate profiling performance. It is well established that this
142 10 km threshold does not introduce a systematic dry bias when comparing against total-column GNSS. Based on the mean
143 radiosonde H_r of 1.51 km observed in this study, moisture decays exponentially (Eq. 8) such that the absolute humidity above
144 10 km is nearly zero. Furthermore, ambient temperatures at this altitude range from -40°C to -50°C, strictly limiting the
145 saturation vapor pressure. Consequently, the residual water vapor between 10 km and the tropopause is thermodynamically
146 constrained to fractions of a millimeter, falling well below the nominal 4% measurement uncertainty of the Vaisala RS41
147 sensor itself.

148

149

150

151 2.2.3 GNSS Data Processing

152 ZTD estimates were derived from the collocated Leica GR50 receiver (station NICO) using the Tefnut PP software (Douša et
153 al., 2014). The processing employed a Precise Point Positioning (PPP) strategy with an elevation cutoff angle of 10°. To
154 account for tropospheric mapping errors, the Vienna Mapping Function 1 (VMF1) was applied. Station coordinates were



155 constrained to the IGS14 reference frame, and satellite orbits and clock corrections were utilized from IGS Ultra-Rapid
156 products. To isolate the ZWD, the ZHD was precisely calculated using continuous, co-located surface pressure observations
157 obtained directly from the Vaisala WXT536 weather transmitter installed at the site, rather than relying on interpolated pressure
158 fields ZTD values were estimated at 15-minute intervals, directly aligning with the temporal resolution of the MWR.
159

160 2.3 Thermodynamic Modeling and Synergistic Retrieval Strategy

161 The conversion of GNSS-derived ZWD to PWV is governed by a proportionality factor, Π , whose accuracy is largely dictated
162 by the T_m . To assess the fidelity of thermodynamic inputs for GNSS meteorology, we evaluated three distinct T_m derivation
163 strategies. For profile-resolving instruments (MWR and RS), T_m values were computed by integrating the vertical profiles of
164 physical temperature, $T(z)$ (K), and absolute humidity, $\rho_v(z)$ (kg m^{-3}). Consistent with Bevis et al. (1992), T_m is defined as the
165 mean temperature of the atmosphere weighted by the water vapor partial pressure, which can be expressed in terms of vapor
166 density as shown in Eq. (4):

$$167 \quad T_m = \frac{\int_{z_{surf}}^{z_{top}} \rho_v(z) dz}{\int_{z_{surf}}^{z_{top}} \frac{\rho_v(z)}{T(z)} dz} \quad (4)$$

168 In practice, the continuous integrals were discretized using the trapezoidal rule from the surface (z_{surf}) to the highest available
169 profile level (z_{top}). This approach assumes linear variation of T and ρ_v between measurement levels. For standalone GNSS
170 retrieval (where no dynamic profiles are available), T_m was derived from the HGPT2 (Hourly Global Pressure and Temperature
171 2) model (Mateus et al., 2021). HGPT2 is an advanced 'blind' empirical model, meaning its outputs are independent of the
172 specific observational year. It is constructed from a comprehensive 20-year historical baseline of atmospheric data from the
173 ERA5 global reanalysis. Unlike standard static climatologies, HGPT2 leverages the full ERA5 spatial resolution ($0.25^\circ \times 0.25^\circ$)
174 and provides temporal resolution at 1-hour intervals for any given Day of Year (DOY). It achieves this by employing a time-
175 segmentation concept, modeling thermodynamic variables via long-term mean values combined with annual, semi-annual, and
176 quarterly periodic functions.

177 To mitigate T_m errors in MWR, a supervised linear regression model was developed to calibrate the MWR observations. For
178 robust independent validation, the collocated dataset was separated into two distinct temporal subsets: the Training Set (April
179 – June 2025), which was used to derive the regression coefficients, and the Validation Set (July – October 2025), which was
180 used exclusively to test the correction's performance on unseen data. A simple linear correction model was fitted to the training
181 data using Ordinary Least Squares (OLS) minimization. The relationship is defined in Eq. (5) as:

$$182 \quad T_{m,corr} = \alpha \cdot T_{m,MWR} + \beta \quad (5)$$

183 where $T_{m,corr}$ is the corrected MWR temperature, $T_{m,MWR}$ is the raw T_m derived from the radiometer and α (slope) and β
184 (intercept) are the learned coefficients minimizing the residual sum of squares between the MWR and RS values. To quantify



185 the benefits of sensor synergy in integrated water vapor estimation, this study defines and contrasts two distinct GNSS PWV
 186 retrieval architectures. The first, “Standard Retrieval” which is a control method utilizes the ZTD_{GNSS} combined with the T_m
 187 derived empirically from the HGPT2 climatological model (Böhm et al., 2015). Second “Synergistic Retrieval” which
 188 proposed method couples ZTD_{GNSS} with a physical T_m derived directly from a collocated MWR. For the synergistic approach,
 189 the dimensionless conversion factor (Π) was calculated dynamically using the MWR-derived T_m following Eq. (6) and Eq. (7).

190
$$PWV = \Pi \cdot ZWD \quad (6)$$

191
$$\Pi = \frac{10^6}{\rho_w R_v [k_2' + (k_3/T_m)]} \quad (7)$$

192
 193 where ρ_w represents the density of liquid water (1000 kg m^{-3}) and R_v is the specific gas constant for water vapor (461.52 J
 194 $\text{kg}^{-1}\text{K}^{-1}$). To assess the sensitivity of the Π to the choice of thermodynamic coefficients, three widely used formulations were
 195 employed in this study, following Davis (1985)/Thayer (1974), Bevis et al. (1994), and Rüeiger (2002), as shown in Table 2:

196 **Table 2.** Refractivity constants used in the sensitivity analysis of the Π factor, based on three commonly adopted formulations.

Method	k_2 (K hPa ⁻¹)	k_3 (K ² hPa ⁻¹)	k_2' (K hPa ⁻¹)
Davis (1985) / Thayer (1974)	64.79	3.776×10^5	16.52
Bevis et al. (1994)	70.40	3.739×10^5	22.13
Rüeiger (2002)	71.295	3.7546×10^5	22.97

197
 198 **2.4 Diagnostic Parameters and Error Analysis**

199 The vertical structure of the atmosphere was analyzed by segregating the dataset into two regimes: the PBL (0–2 km), where
 200 water vapor is concentrated, and the Free Troposphere (> 2 km). Additionally, the scale height (H_v) was calculated to quantify
 201 the vertical distribution of moisture. This parameter is crucial because it provides a single, representative value for the rate at
 202 which water vapor decreases with altitude, which is a key factor in understanding atmospheric stability, cloud formation, and
 203 radiative transfer processes. H_v was derived for both RS and MWR by fitting an exponential decay function (Eq. 8) to the
 204 absolute humidity profile (ρ_v). This curve fitting was deliberately restricted to the lowest 4 km of the atmosphere because this
 205 layer contains the vast majority (>90%) of the tropospheric water vapor mass. As established in climatological studies (e.g.,
 206 Trenberth et al., 2005; Weaver and Ramanathan, 1995), atmospheric water vapor decays exponentially with a typical scale
 207 height of 1.5 to 2.5 km. Above 4 km, moisture levels approach the noise floor of both the MWR and the RS sensors, and the
 208 profile frequently deviates from a standard exponential decay due to complex layering or subsidence inversions. Forcing an
 209 exponential fit over the entire 10 km column causes the algorithm to heavily weight near-zero, noisy upper-tropospheric values,
 210 which mathematically degrades the curve fit for the boundary layer where the bulk mass actually resides (Tomasi, 1984).



211 Therefore, the 4 km limit is a necessary mathematical boundary to ensure a physically meaningful fit.

$$212 \quad \rho_v(z) = \rho_{v,0} \cdot \exp\left(-\frac{z}{H_v}\right) \quad (8)$$

213 where $\rho_v(z)$ is the absolute humidity at height z , and $\rho_{v,0}$ is the surface humidity. Furthermore, the scale height metric
 214 fundamentally assumes the atmosphere conforms to a well-behaved exponential decay. During complex meteorological
 215 states—such as deep convective mixing, strong elevated moist layers, or severe shallow inversions—the true vertical moisture
 216 distribution breaks this exponential assumption. Forcing a mathematical fit onto these non-exponential profiles yields
 217 physically meaningless artifacts. Therefore, a Quality Assurance filter was applied, bounding the analysis to the physically
 218 realistic range of $0.1 \text{ km} < H_v < 4.0 \text{ km}$. Profiles yielding values outside this range were discarded because they indicate the
 219 underlying exponential model itself is invalid for that specific atmospheric profile, preventing artificial statistical skewing in
 220 the instrument intercomparison. Profiles yielding H_v values outside the physically realistic range of 0.1 to 4.0 km were excluded
 221 from the statistical analysis. To evaluate the performance limitations of standard climatological models under varying
 222 hygrometric conditions, the systematic error (ΔPWV) was defined as the residual between the synergistic and standard
 223 approaches (Eq. 9):

$$224 \quad \Delta PWV = PWV_{Synergistic} - PWV_{Standard} \quad (9)$$

225 The dataset was stratified into discrete bins of 5 mm PWV to isolate regimes of thermodynamic severity. Within each bin, the
 226 mean bias and $\pm 1\sigma$ uncertainty were computed. These statistics were utilized to determine the "Critical Error Culmination,"
 227 defined herein as the specific hygrometric threshold where the systematic model error exceeds 1 mm. Finally, the propagation
 228 of thermodynamic uncertainty into the moisture retrieval was quantified via linear regression analysis. This compared the
 229 relative error in T_m (HGPT2 vs. MWR) against the resulting relative error in PWV, serving as an empirical verification of the
 230 theoretical sensitivity approximation given in Eq. (10):

$$231 \quad \frac{\Delta PWV}{PWV} \approx \frac{\Delta T_m}{T_m} \quad (10)$$

232 3 Results

233 3.1 Temperature and Humidity Profile Validation

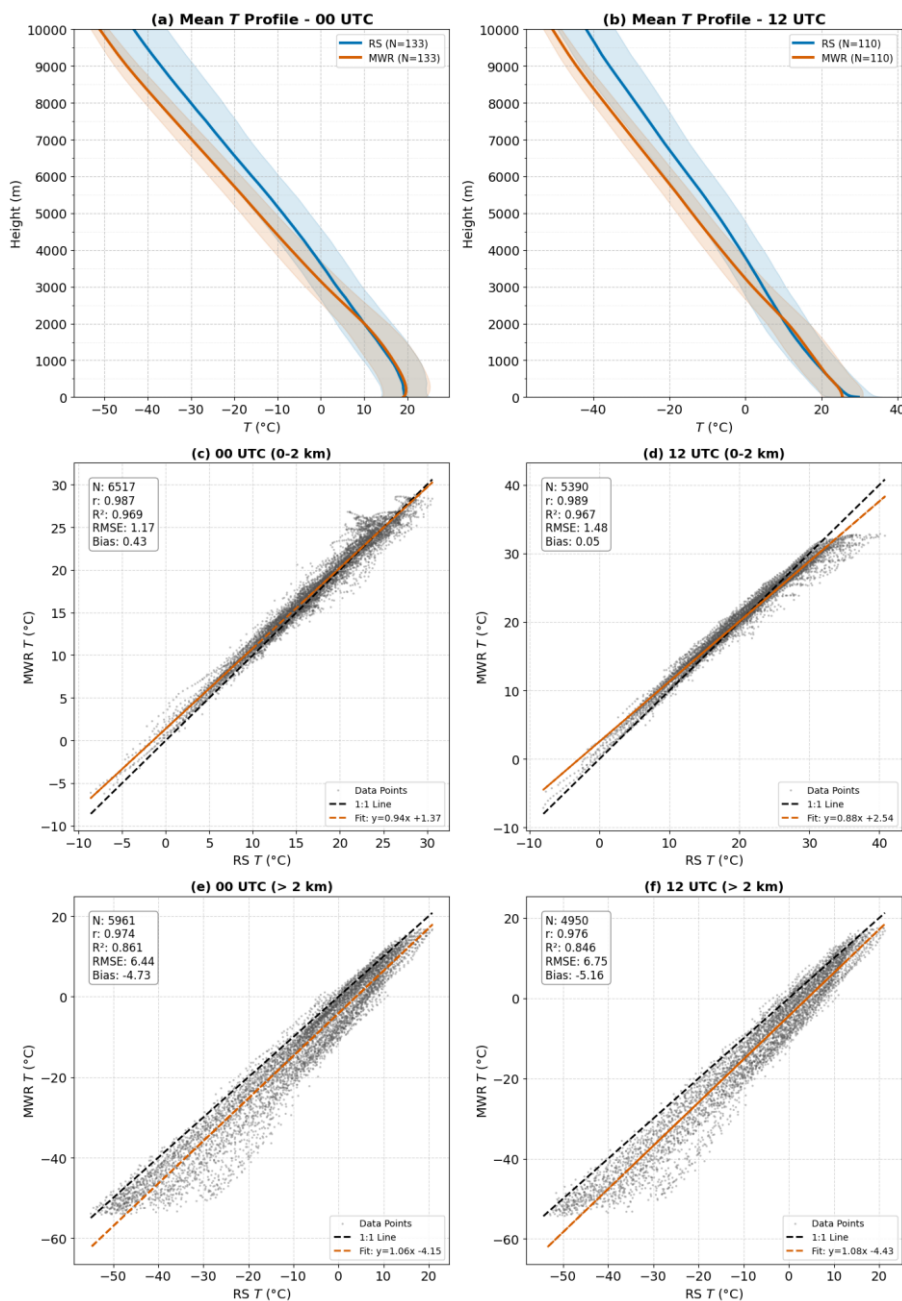
234 MWR-retrieved temperature T and ρ_v profiles were validated against collocated RS observations at 00:00 UTC and 12:00 UTC
 235 during March–October 2025. Profiles were stratified into the planetary boundary layer (PBL; 0–2 km) and free troposphere
 236 (>2 km), as shown in Figs. 2 and 3. Mean vertical temperature profiles show agreement between MWR and RS (Fig. 2a–b).
 237 In the boundary layer (0–2 km), MWR retrieves temperature with high precision ($r > 0.98$, $RMSE < 1.5 \text{ K}$). Above 2 km, a cold
 238 bias is observed in the MWR retrieval, reaching -5.16 K at 12 UTC (Fig. 2f). Despite this bias, the linearity remains strong
 239 ($r \approx 0.97$), indicating the sensor captures relative thermal variations aloft despite the absolute offset. This confirms the trend
 240



241 observed in the mean profiles, where the MWR underestimates temperatures in the mid-to-upper troposphere. Consequently,
242 the RMSE increases substantially to approximately 6.4–6.7°C. The stark contrast in accuracy between the lower and upper
243 troposphere is a known characteristic of ground-based microwave radiometry (Parde et al., 2025; Pakkattil et al., 2025). The
244 high accuracy below 2 km is attributed to the high information content of the opaque V-band channels (51–58 GHz), whose
245 weighting functions peak near the surface. Above 2 km, these weighting functions broaden significantly, reducing vertical
246 resolution and causing a "smearing" effect where the instrument provides a volume-averaged temperature rather than a precise
247 point measurement. The observed cold bias is likely a result of the retrieval algorithm (e.g., neural network) relying heavily
248 on a climatological *a priori* dataset that does not perfectly represent the thermal conditions of the transition season observed,
249 or systematic offsets in the radiative transfer model (absorption coefficients) used for training.

250 The mean ρ_v profiles (Figs. 3a–b) show the expected exponential decrease of moisture with height. At 00 UTC, the profiles
251 align reasonably well. However, at 12 UTC, the MWR profile exhibits a structural deviation between 1–2 km, failing to capture
252 the smooth moisture gradient recorded by the RS. This discrepancy may be attributed to the MWR's limited vertical resolution
253 during periods of active daytime mixing or complex humidity layering. The retrieval of humidity in the lower atmosphere
254 shows moderate agreement but is less accurate than the temperature retrievals. Performance is notably better at night (00 UTC)
255 with r of 0.878 and RMSE of 1.98 g m⁻³. At 12 UTC, the correlation drops to 0.744, and the scatter increases (RMSE =2.31 g
256 m⁻³). A negative bias persists at both times (–0.51 g m⁻³ at 00 UTC and –0.91 g m⁻³ at 12 UTC), indicating a tendency for the
257 MWR to underestimate moisture content in the boundary layer, particularly during the day. Surprisingly, the statistical linearity
258 for ρ_v improves slightly or remains stable above 2 km, likely due to the lower overall magnitude of humidity at these heights.
259 The correlation coefficients remain stable (~0.87). In contrast to the lower levels, the bias shifts to slightly positive values
260 (0.23 g m⁻³ at 00 UTC and 0.46 g m⁻³ at 12 UTC), suggesting a slight moist bias in the MWR retrievals aloft. The linear fits
261 (Figs. 3e–f) align closely with the 1:1 line, with slopes near unity (0.90 and 1.00), indicating that the MWR effectively captures
262 the free tropospheric humidity trends despite the lower absolute values. The difficulty in retrieving accurate ρ_v profiles,
263 particularly at 12 UTC, stems from the limited vertical resolution of the K-band channels (22–31 GHz). Unlike temperature
264 profiling, humidity profiling offers very few independent degrees of freedom (typically <3), making it difficult for the MWR
265 to resolve sharp vertical gradients often present at the top of the convective boundary layer during the daytime. The structural
266 deviation and underestimation are common issues linked to the "smoothing" error inherent in passive radiometry, where sharp
267 moisture inversions are averaged out. Furthermore, the persistent bias suggests potential uncertainties in the water vapor
268 absorption models (spectroscopic parameters) or non-representative training data used in the retrieval algorithm.

269



270

271 Figure 2. Comparison of radiosonde and microwave radiometer (MWR) temperature profiles: (a–b) Mean vertical temperature
 272 (T) profiles at 00 and 12 UTC with variability shading; (c–f) Scatter comparisons for the lower (0–2 km) and upper (>2 km)
 273 atmosphere at both times.

274

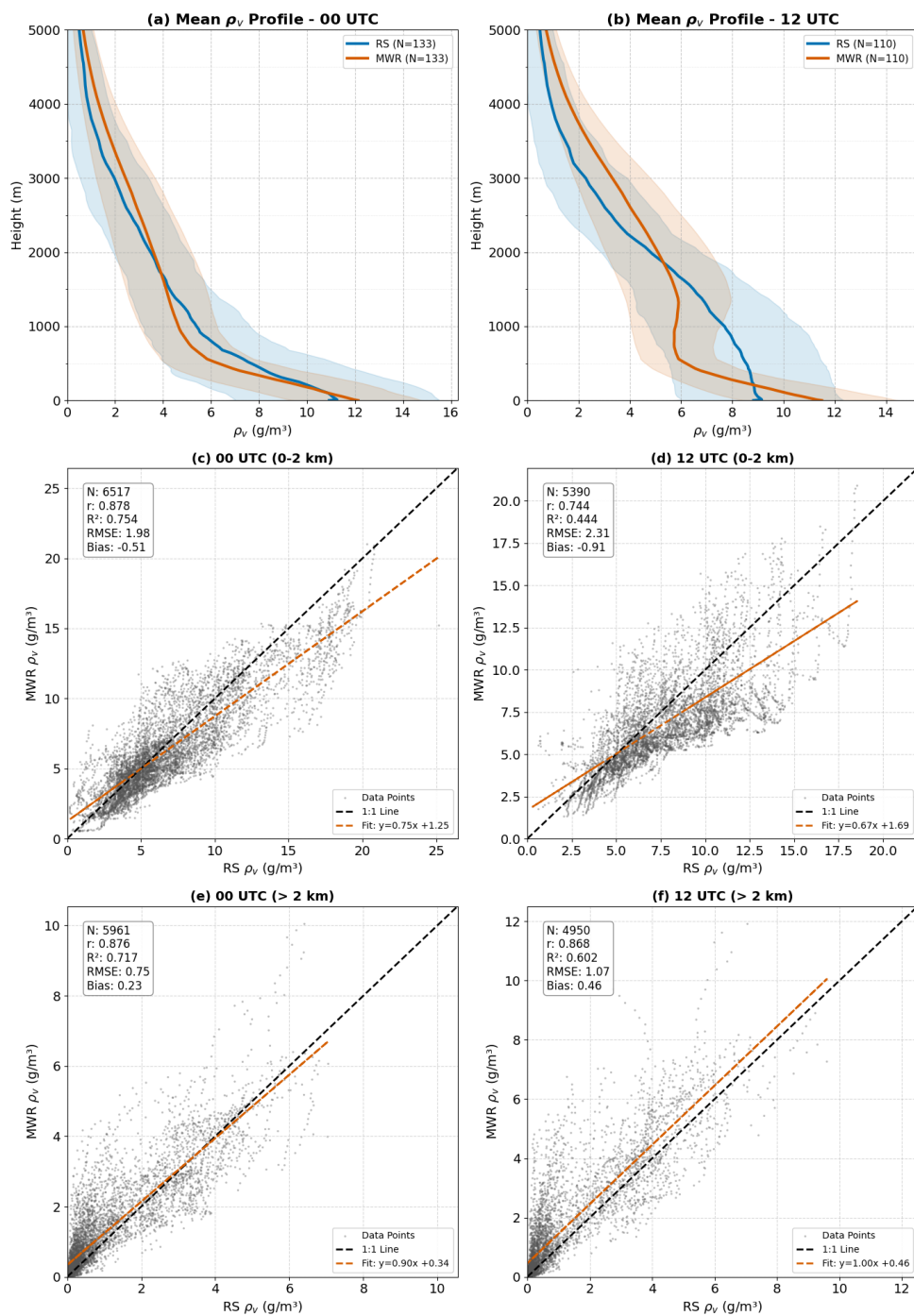


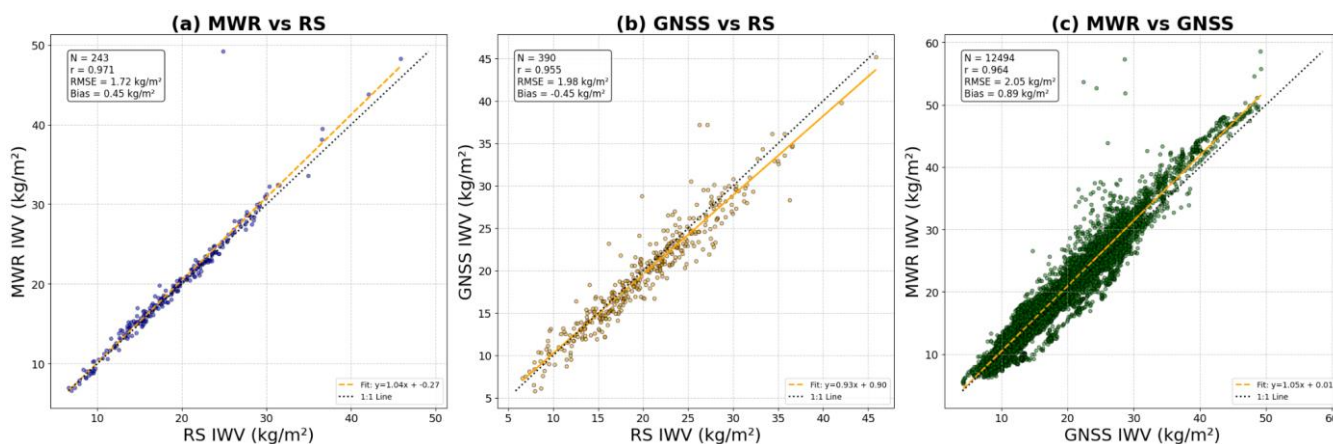
Figure 3. Comparison of radiosonde and microwave radiometer (MWR) absolute humidity (ρ_v) profiles: (a–b) Mean vertical ρ_v profiles at 00 and 12 UTC with variability shading; (c–f) Scatter comparisons for the lower (0–2 km) and upper (>2 km) atmosphere at both times.

275
276
277
278

279 3.2 Integrated Water Vapor (IWV) and Scale Height (H_v) Validation



280 Unlike vertical profiling, the MWR excels in measuring total column quantities. The comparison with RS yields an excellent
 281 correlation ($r=0.971$) and a low RMSE of 1.72 kg m^{-2} . This performance disparity—superior IWV versus degraded profiles—
 282 confirms that while the sensor cannot resolve vertical structural details due to smoothing error, the radiometric brightness
 283 temperature in the K-band remains strictly proportional to the total precipitable water mass. The GNSS-derived IWV shows a
 284 slight negative bias relative to RS (-0.45 kg m^{-2}), whereas the MWR exhibits a positive bias ($+0.45 \text{ kg m}^{-2}$). The cumulative
 285 offset observed in the MWR-GNSS intercomparison ($+0.89 \text{ kg m}^{-2}$) highlights the systematic differences in calibration and
 286 retrieval assumptions between active (GNSS) and passive (MWR) techniques. The GNSS underestimation is likely driven by
 287 errors in the T_m derived from the static HGPT2 model, a hypothesis further explored in Section 3.4. The limitation of passive
 288 microwave profiling is most evident in the derivation of the water vapor H_v . The MWR-derived H_v shows negligible correlation
 289 with RS ($r=0.25$) and a systematic positive bias of 0.62 km . As detailed in Figure 5, the MWR distribution is artificially shifted
 290 toward higher values. This "stretching" effect is a direct artifact of the smoothing error; by failing to resolve the rapid moisture
 291 decrease at the PBL top, the retrieval algorithm smears the moisture profile upward, mathematically inflating the calculated e-
 292 folding depth. Therefore, while MWR is a primary standard for IWV, it should not be relied upon for characterizing vertical
 293 moisture compactness without synergistic constraints.

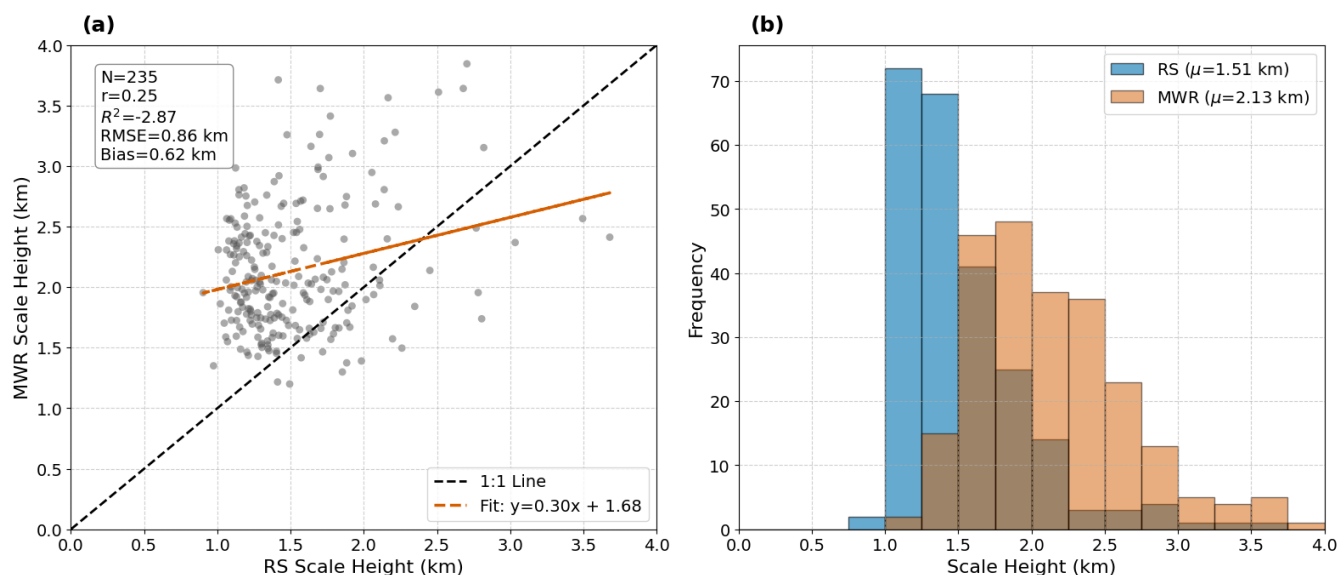


294 **Figure 4.** Intercomparison of integrated water vapour (IWV) retrieved from Microwave Radiometer (MWR), GNSS, and Radiosonde
 295 observations. (a) MWR IWV versus radiosonde IWV, (b) GNSS IWV versus radiosonde IWV, and (c) MWR IWV versus GNSS IWV.
 296

297 The water vapor H_v , which describes the exponential decay of moisture with altitude, was calculated for both RS and MWR
 298 profiles. The comparison is shown in Fig. 5. Unlike the IWV, the derived scale height from MWR shows poor agreement with
 299 RS observations (Fig. 5a). The correlation is weak ($r=0.25$), and the coefficient of determination is negative ($R^2=-2.87$),
 300 indicating that the MWR-derived scale height has no predictive power for the true atmospheric scale height. The MWR
 301 consistently overestimates H_v , with a significant positive bias of 0.62 km and a regression slope (0.30) that is far flatter than
 302 the 1:1 line. The histograms (Fig. 5b) further elucidate this discrepancy. The RS scale heights (blue bars) follow a narrow
 303 distribution centered around a mean (μ) of 1.51 km , typical for the study region. In contrast, the MWR distribution (orange
 304 bars) is much broader and shifted significantly to higher values ($\mu=2.13 \text{ km}$). The MWR rarely computes scale heights below



305 1.5 km, whereas the RS frequently observes compact moisture layers with scale heights near 1.0–1.2 km. The failure of the
 306 MWR to accurately derive scale height is a direct consequence of the physical limitations of passive microwave remote sensing.
 307 H_v is highly sensitive to the sharp vertical gradient of humidity ($\partial z/\partial \rho_v$) at the top of the boundary layer. The K-band channels
 308 (22–31 GHz) utilized for humidity profiling possess broad weighting functions, which limits the vertical degrees of freedom
 309 to typically fewer than three. Because the MWR lacks the vertical resolution to capture sharp moisture inversions, the retrieval
 310 algorithm mathematically smears the moisture mass upward. This inherent smoothing effect artificially elongates the vertical
 311 moisture profile, effectively increasing the calculated e-folding depth. This confirms that while the MWR is a robust standard
 312 for total column water (IWV), a single-parameter exponential fit like H_v is inadequate for characterizing vertical moisture
 313 compactness using passive radiometry. This result highlights a critical limitation: while MWR is excellent for total column
 314 water (IWV), it is not reliable for characterizing the vertical compactness of the moisture layer (H_v).



315
 316 **Figure 5:** Comparison of scale height from radiosonde (RS) and microwave radiometer (MWR): (a) Scatter plot with 1:1 line and linear fit,
 317 including summary statistics; (b) Frequency distributions showing mean scale heights for RS and MWR.

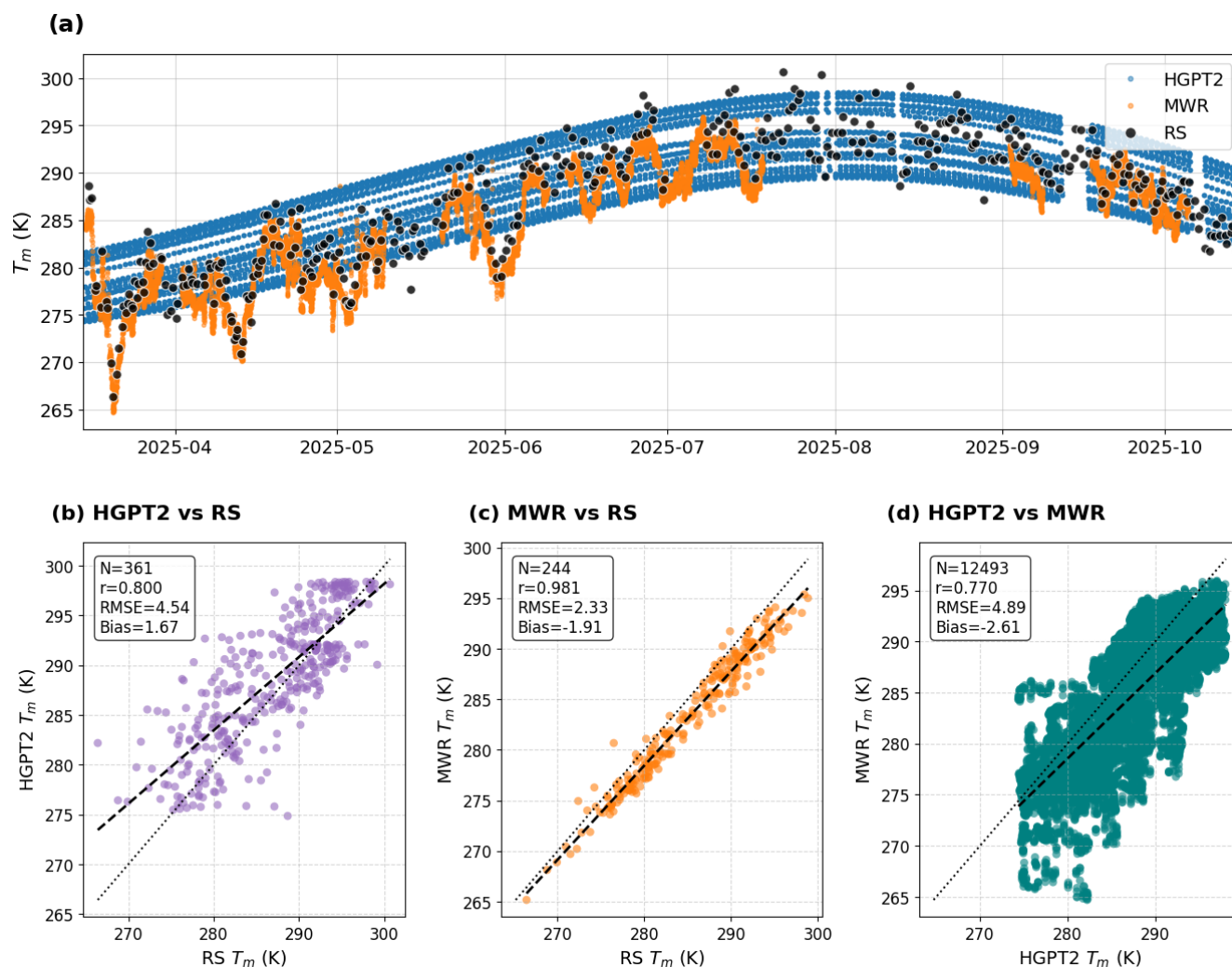
318

319 3.3 Weighted Mean Temperature (T_m) Validation

320 The accurate estimation of the T_m is critical for converting GNSS-derived ZWD into PWV. The performance of T_m derived
 321 from the MWR and the empirical GPT2w model (HGPT2) was evaluated against RS measurements, which serve as the "ground
 322 truth." The results are presented in Fig. 6. The time series (Fig. 6a) illustrates the seasonal evolution of T_m from April to October
 323 2025. The Radiosonde observations (black dots) show significant variability, capturing synoptic-scale weather fluctuations.
 324 The MWR-derived T_m (orange dots) tracks these fluctuations with remarkable precision, overlaying the RS points almost
 325 perfectly. In stark contrast, the HGPT2 model (blue dots) provides a smooth, climatological curve. While it captures the general
 326 seasonal trend, it completely misses the day-to-day thermodynamic variability, often overestimating T_m during cooler transient



327 events and underestimating it during warmer anomalies. The empirical model shows only moderate performance ($r=0.800$)
328 with a substantial spread (RMSE = 4.54 K). A systematic positive bias of 1.67 K indicates that HGPT2 generally overestimates
329 the atmospheric temperature profile in this region. The scatter plot reveals a diffuse, "cloud-like" distribution, confirming its
330 inability to capture real-time atmospheric dynamics. The MWR demonstrates superior performance, achieving a near-perfect
331 correlation ($r=0.981$). The RMSE is significantly reduced to 2.33 K, which is nearly half the error of the empirical model.
332 Interestingly, the MWR exhibits a negative bias of -1.91 K, suggesting a systematic underestimation of T_m . Crucially, this bias
333 does not originate in the free troposphere, but rather in the planetary boundary layer (0–3 km). Since T_m is weighted by water
334 vapor pressure, this "cold bias" indicates the MWR is underestimating the intense near-surface heating or the sharp lapse rates
335 characteristic of the Nicosia environment. Despite this offset, the tight linearity indicates that MWR is an excellent source for
336 capturing real-time T_m variations. Comparing the large dataset of MWR against HGPT2 ($N=12,493$) confirms the discrepancy
337 between dynamic and static modeling. The correlation is lower ($r=0.770$) and the scatter is large (RMSE = 4.89 K), further
338 proving that static empirical models are insufficient for high-precision GNSS meteorology compared to dynamic radiometer
339 measurements. The accuracy of PWV retrieval from GNSS is linearly dependent on the error in T_m . A standard rule of thumb
340 states that a 1% error in T_m translates to roughly a 1% error in PWV. By switching from a static model (HGPT2, ~ 4.5 K error)
341 to a dynamic sensor (MWR, ~ 2.3 K error), the uncertainty in the GNSS water vapor product is effectively halved. This
342 validates the "synergistic" approach of using collocated MWR thermal data to process GNSS signals.



343
344
345
346
347

Figure 6. Comparison of weighted mean temperature (T_m) derived from HGPT2, MWR, and Radiosonde (RS) during March–November 2025. (a) Time series of T_m estimates from all three sources. (b–d) Scatter plots showing statistical comparisons between: (b) HGPT2 vs. RS, (c) MWR vs. RS, and (d) HGPT2 vs. MWR.

348 3.4 Diagnostic Analysis of Thermodynamic Errors

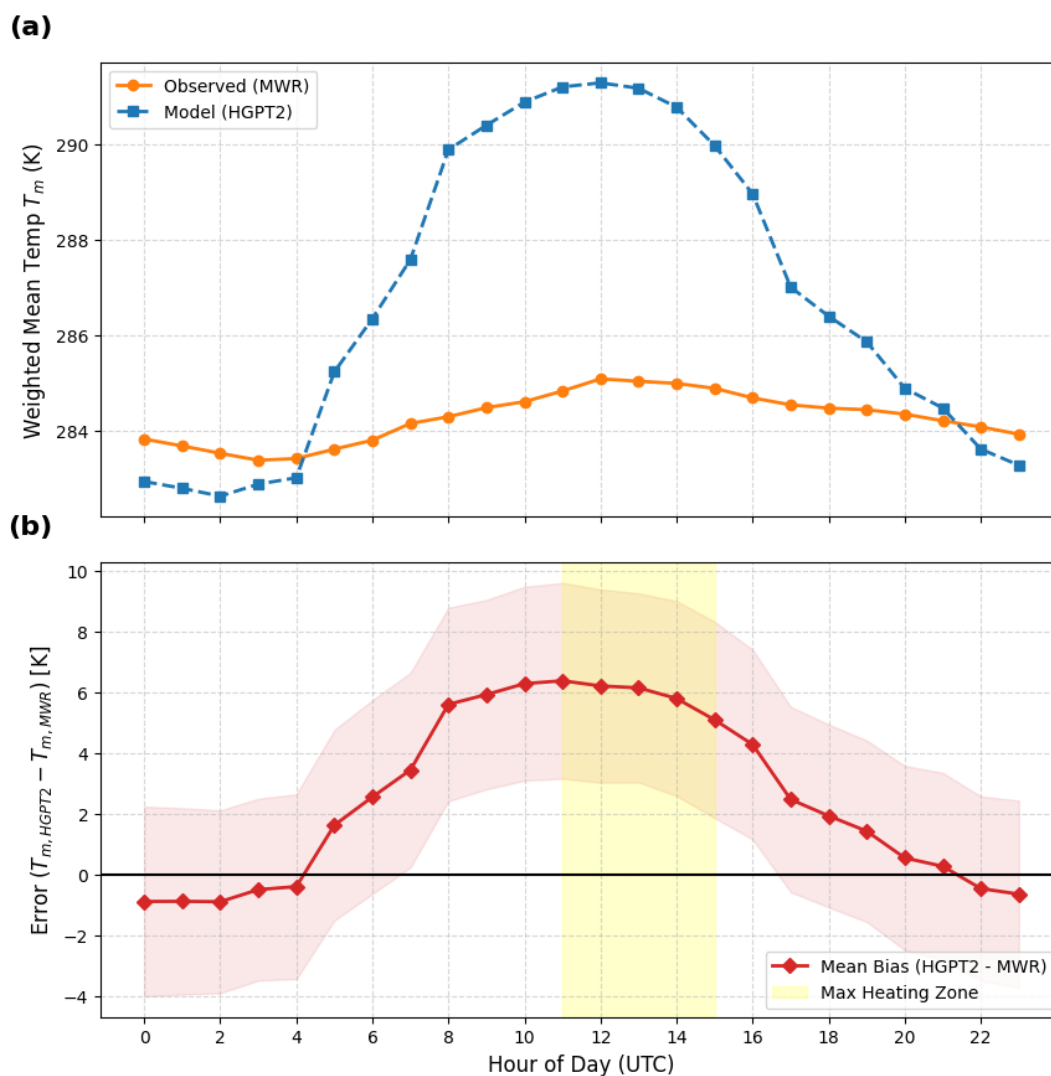
349 3.4.1 Diurnal Bias Amplification in Static Models

350 To pinpoint the physical origin of the HGPT2 model's deficiency, a diurnal cycle analysis was performed (Fig. 7). While the
351 previous statistical metrics indicated a general positive bias, the temporal breakdown in Fig. 7a reveals that this error is not
352 uniform, but is driven by a fundamental misrepresentation of atmospheric thermodynamics. The MWR-derived T_m (orange
353 line) exhibits a physically realistic, dampened diurnal amplitude of approximately 1.5 K. This stability reflects the high thermal



354 inertia of the tropospheric column, which does not heat rapidly in response to surface insolation. In stark contrast, the HGPT2
355 model (blue line) displays an exaggerated diurnal wave with an amplitude exceeding 8.5 K, peaking synchronously with solar
356 noon (12:00 UTC). This exaggerated daytime amplitude suggests that the empirical model's periodic functions are overly
357 sensitive to surface skin temperature (T_s). More importantly, because T_m is fundamentally defined as a moisture-weighted
358 integral, the diurnal evolution of specific humidity plays a critical, coupled role in this error. During the hours of peak solar
359 insolation (11:00–14:00 UTC), the coastal environment experiences active convective mixing and the onset of the sea breeze,
360 which dramatically alters the vertical distribution of water vapor. If the underlying reanalysis climatology fails to adequately
361 resolve the sharp moisture capping inversion at the top of the daytime planetary boundary layer (PBL), it will misrepresent the
362 T_m weighting function. Specifically, if the model traps too much moisture near the intensely heated surface—or fails to capture
363 the thermodynamic decoupling between the turbulent PBL and the stable free troposphere — the integral will
364 disproportionately weight the hottest atmospheric layers. This coupled temperature-humidity mechanism physically manifests
365 as the severe 'noon ballooning' effect observed in Fig. 7b, where the systematic bias surges to over +6 K. This demonstrates
366 that high-precision GNSS meteorology requires synergistic MWR data to capture both the true thermal stability and the
367 dynamic vertical moisture weighting of the atmosphere.

368



369
370
371
372
373

Figure 7. Diurnal variation of weighted mean atmospheric temperature T_m derived from microwave radiometer (MWR) observations and HGPT2 model simulations (top panel). The bottom panel shows the corresponding hourly mean bias ($T_{m,HGPT2} - T_{m,MWR}$), with shaded envelopes indicating variability. The yellow shaded region highlights the period of maximum daytime heating.

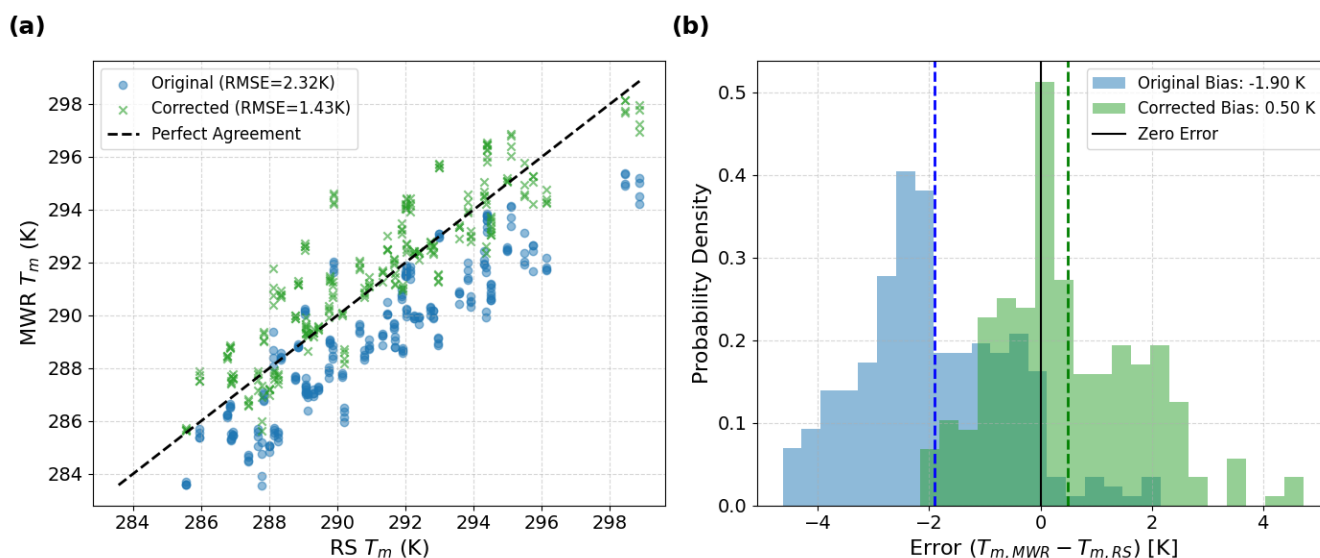
374 3.4.2 Calibration and Bias Correction of MWR T_m

375 Fig. 8 presents a statistical validation of the MWR derived T_m against co-located RS observations. The analysis highlights the
376 necessity and efficacy of a linear bias correction scheme to improve GNSS-PWV conversion accuracy. The scatter plot (Fig.
377 2a) reveals a distinct systematic deviation in the original MWR retrieval relative to the RS reference. The data points
378 consistently fall below the 1:1 identity line, indicating a negative bias in the raw MWR T_m product. The original RMSE is 2.32
379 K. This error is largely driven by the systematic offset rather than random scatter, as evidenced by the high linearity (R^2) of



380 the relationship. The thermodynamic profiles were retrieved using the manufacturer's standard Neural Network (NN)
 381 algorithm, trained on Region historical RS data.

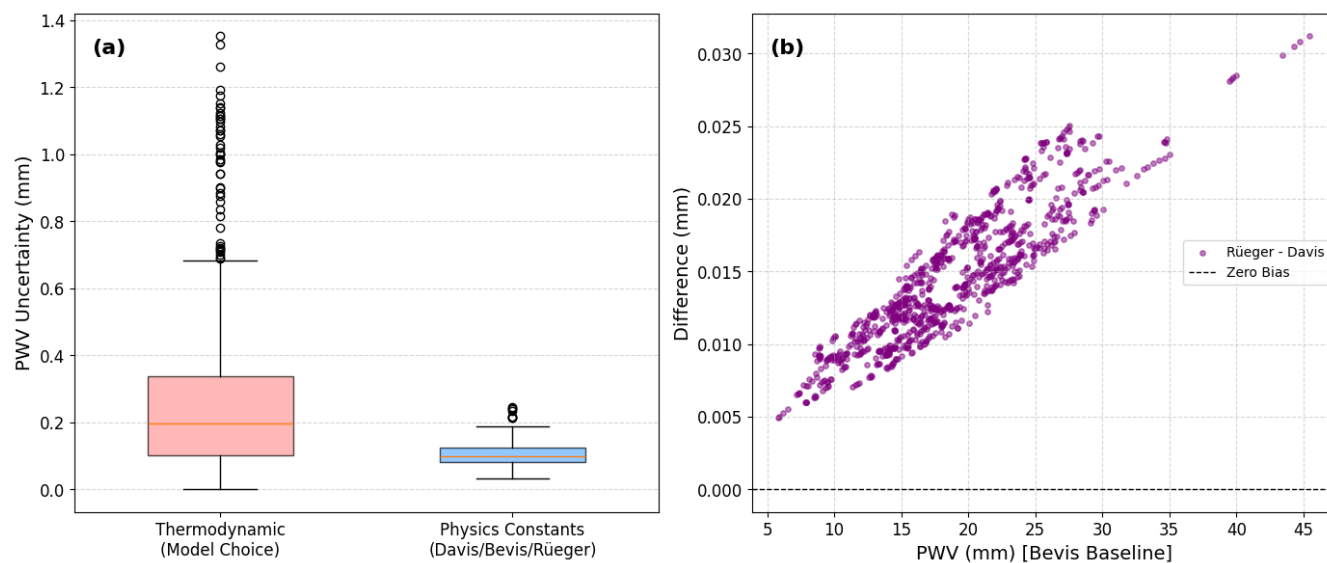
382 The Probability Density Function (PDF) of the errors ($T_{m,MWR} - T_{m,RS}$) in Fig. 8b clearly visualizes the bias shift. The pre-
 383 correction distribution is non-Gaussian and shifted significantly to the negative domain, with a mean bias (μ) of -1.90 K. In
 384 the context of GNSS meteorology, a T_m error of ≈ 2 K translates to a relative PWV error of approximately 0.7–1.0%. For
 385 climate monitoring, this represents a significant systematic dry bias. Applying the linear correction model ($T_{m,corr} = \alpha T_{m,raw} + \beta$)
 386 successfully re-centers the error distribution. The post-correction bias is reduced to 0.50 K, and the histogram aligns
 387 symmetrically around the zero-error line. The correction reduces the RMSE to 1.43 K, which is consistent with the theoretical
 388 accuracy limit of ground-based radiometric profiling (typically 1–2 K). The remaining spread (width of the green histogram)
 389 represents the random error component, likely attributable to instrumental noise and the imperfect spatiotemporal matching
 390 between the instantaneous MWR zenith view and the drifting radiosonde balloon. The correction methodology effectively
 391 removes the systematic instrumental bias without artificially compressing the natural variability of the atmosphere. The
 392 reduction of RMSE by $\sim 38\%$ (from 2.32 K to 1.43 K) confirms that site-specific calibration of T_m is a mandatory processing
 393 step for generating climate-quality GNSS-PWV datasets.



394 **Figure 8.** Evaluation of weighted mean temperature T_m correction against Radiosonde (RS) observations. (a) scatter plots of original and
 395 bias-corrected MWR-derived T_m versus RS T_m , with the dashed line indicating perfect agreement. (b) presents the probability density of
 396 errors ($T_{m,MWR} - T_{m,RS}$) before and after correction, demonstrating a substantial reduction in cold bias and RMSE.
 397
 398



399 **3.4.3 Uncertainty Budget Analysis**



400 **Figure 9.** (a) PWV uncertainty attributed to thermodynamic assumptions and to the choice of refractivity constants. (b) Difference in GNSS-
 401 derived PWV resulting from the use of alternative refractivity constant formulations relative to Bevis et al. (1994).
 402

403
 404 In standard GNSS network processing, the largest source of PWV uncertainty is often the interpolation or modeling of
 405 surface pressure required to calculate the ZHD (Van Malderen et al., 2022). However, the CYGMEN observatory setup
 406 mitigates this spatial interpolation error by utilizing the co-located Vaisala WXT536 sensor, which has a stated pressure
 407 accuracy of ± 0.5 hPa. A 0.5 hPa pressure uncertainty propagates to approximately 1.15 mm of error in the ZHD. After applying
 408 the Π conversion factor, this restricts the pressure-induced PWV uncertainty to roughly ± 0.17 mm. Because this high-precision
 409 localized pressure data effectively minimizes ZHD uncertainty, the accuracy of the T_m parameterization emerges as the
 410 dominant remaining variable in the PWV error budget for this site.

411 To decouple the error contributions in the GNSS-PWV retrieval chain, a component-wise uncertainty analysis was
 412 performed focusing on the conversion factor, Π . Two primary sources of uncertainty were isolated: the thermodynamic
 413 parameterization of T_m and the selection of atmospheric refractivity constants (k_2' , k_3). As illustrated in Fig. 9(a), the
 414 uncertainty introduced by the T_m estimation strategy significantly outweighs the influence of the physical constants.
 415 Specifically, the stochastic variability from modeling T_m (comparing HGPT2 climatology against direct radiometric
 416 observation) results in a retrieval error of approximately 1–2 mm. In contrast, the uncertainty associated with the choice of
 417 refractivity coefficients—defined here as the maximum divergence between the historical Davis et al. (1985), the standard
 418 Bevis et al. (1994), and the updated Rüeger (2002) formulations—remains an order of magnitude smaller. Fig. 9(b) further
 419 resolves the impact of the refractivity constants, showing the differential bias between the oldest (Davis) and newest (Rüeger)
 420 standards. The relationship is linear and proportional to the total water vapor content, consistent with a scaling of the Π factor.



421 While the transition to the Rüeiger (2002) constants introduces a systematic positive shift, the magnitude of this correction
422 (typically <0.2 mm for standard loading) is negligible for synoptic meteorological applications compared to the noise induced
423 by T_m errors. However, for long-term climatological trend analysis where stability is paramount, consistent adherence to the
424 Rüeiger (2002) standard is recommended to eliminate this small, but persistent systematic bias. Overall, the correction of the
425 T_m is 2.5 times more important than selection of the constant.

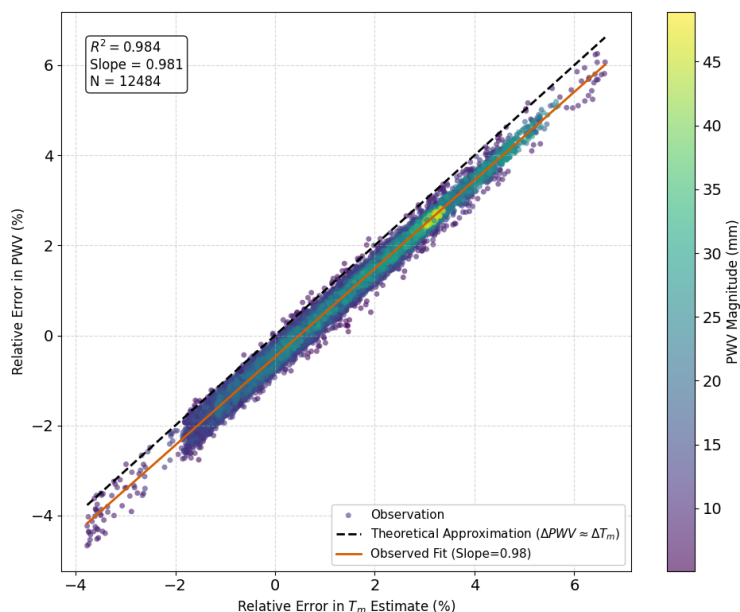
426

427 3.5 Error Propagation and Synergistic Retrieval Assessment

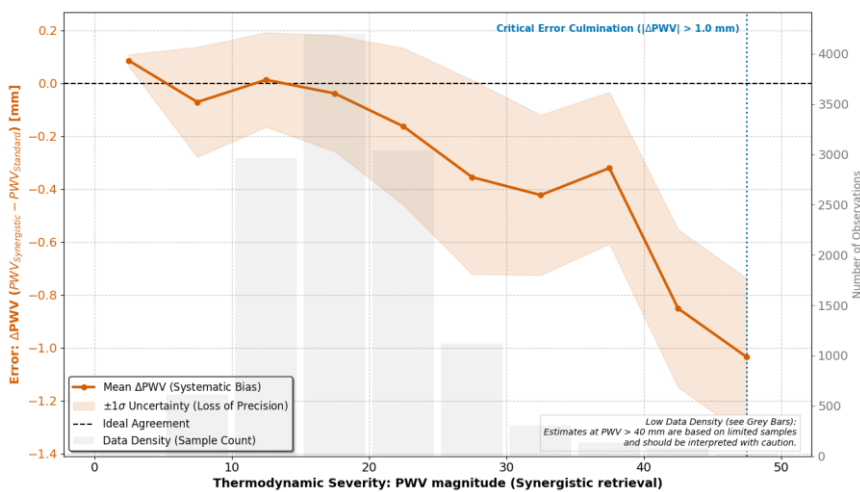
428 In this section, the PWV was derived using bias-corrected mean temperature (T_m) and constant values based on the study by
429 Rüeiger (2002), as mentioned in the Sect. 3.4. The impact of T_m errors on the final PWV product was analyzed to quantify the
430 benefits of the synergistic retrieval method. Fig. 10 visualizes the direct relationship between the relative error in T_m and the
431 resulting relative error in PWV. The plot reveals a strictly linear relationship ($R^2=0.984$) with a slope of 0.981. This confirms
432 the theoretical approximation that $(\Delta PWV/PWV) \approx (\Delta T_m/T_m)$. The color gradient indicates that this linear error propagation
433 holds true across all PWV magnitudes (from <10 mm to >45 mm). This implies that temperature errors propagate directly into
434 moisture errors regardless of the humidity level, making accurate T_m crucial at all times. Fig. 11 investigates the systematic
435 difference (ΔPWV) between the synergistic retrieval (using MWR T_m) and a standard retrieval (using empirical T_m) as a
436 function of thermodynamic severity (PWV magnitude). For drier conditions (PWV < 25 mm), the difference is minimal (near
437 zero), and the uncertainty (shaded region) is low. This suggests that for low humidity, the choice of T_m source is less critical.
438 As atmospheric moisture increases (> 25 mm), a significant negative bias emerges. The curve dips sharply, reaching nearly
439 -1.0 mm at extreme humidity (45+ mm). The "Critical Error Culmination" marker indicates that beyond 45 mm, the
440 discrepancy exceeds 1.0 mm. The fact that the bias magnitude scales directly with total PWV provides physical confirmation
441 that the error source is located in the boundary layer, where the bulk of the water vapor resides. The growing negative bias
442 demonstrates that standard GNSS processing (using static models like HGPT2) systematically overestimates water vapor
443 during extreme events compared to the more accurate synergistic method. Rather than extrapolating these localized errors to
444 regional hydrological impacts, we emphasize the primary empirical observation: the systemic deviation of the standard
445 empirical model scales proportionally with the magnitude of the PWV regime. Crucially, this systematic overestimation of
446 moisture during extreme events is deeply intertwined with the diurnal cycle of the local atmosphere. As previously established
447 (Fig. 7), the static HGPT2 model displays an exaggerated diurnal wave with an amplitude exceeding 8.5 K. Because the static
448 model fails to account for the thermodynamic decoupling between the heated boundary layer and the cooler free troposphere
449 during the day, this T_m error artificially inflates the amplitude of the GNSS-derived PWV diurnal cycle during peak solar
450 insolation. By utilizing the synergistic retrieval approach, this spurious daytime moisture amplification is effectively mitigated.
451 While further multi-site, long-term studies are required to assess the broader impacts on regional operational forecasting, our



452 localized dataset clearly indicates that integrating real-time MWR thermal data successfully removes diurnal artifacts and
 453 reduces systematic measurement biases at this site.
 454



455
 456 **Figure 10.** Driver of model failure: Impact of weighted mean temperature (T_m) accuracy on PWV retrieval.
 457



458
 459 **Figure 11.** Systematic breakdown and instability of the Standard GNSS model under extreme thermodynamic conditions.
 460



461 **4 Discussions**

462 The results of this study necessitate a fundamental re-evaluation of how thermodynamic path delays are parameterized in
463 GNSS meteorology, particularly within thermodynamically complex, semi-arid coastal environments like the Eastern
464 Mediterranean (EM). The pronounced failure of the static HGPT2 model to capture the diurnal T_m cycle reveals a structural
465 limitation inherent to empirical modeling. The observed "noon ballooning" effect is not merely a statistical anomaly; it
466 represents a physical disconnect. Static empirical models rely heavily on T_s , effectively assuming that intense skin-level heating
467 propagates uniformly through the atmospheric column. This assumption critically breaks down during the daytime in the EM,
468 where the turbulent planetary boundary layer (PBL) aggressively decouples from the stable free troposphere. Furthermore, the
469 failure of the reanalysis climatology to properly resolve the sharp moisture capping inversion during the onset of the daytime
470 sea-breeze fundamentally corrupts the moisture-weighted T_m integral. Ground-based microwave radiometry overcomes this
471 structural blindness by directly measuring the integrated thermal emissions of the column.

472 However, the performance of the MWR in this study highlights the duality of passive microwave remote sensing: it is highly
473 proficient at retrieving integral quantities but degrades severely when resolving differential or gradient-based parameters. The
474 successful reduction of the T_m RMSE via site-specific linear correction confirms that the MWR's K-band and V-band channels
475 effectively capture the true thermal inertia of the troposphere. The initial systematic cold bias observed aloft is a known artifact
476 of ill-posed neural network retrievals, which are heavily constrained by historical training datasets that often fail to capture
477 localized, transition-season lapse rates. Conversely, the complete failure of the MWR to derive a physically realistic water
478 vapor scale height (H_v) exposes the "smoothing error" inherent to passive radiometry. Because the broad weighting functions
479 of the K-band channels cannot resolve sharp boundary layer moisture inversions, the retrieval algorithm mathematically smears
480 the moisture mass upward. This confirms that while MWR serves as a robust standard for total column mass, researchers must
481 exercise extreme caution when utilizing its smoothed profiles to characterize vertical moisture compactness.

482 While this study relies on a single-site, multi-month dataset, the physical mechanisms identified have broad relevance beyond
483 the Nicosia region. The Eastern Mediterranean serves as a highly representative climatic hotspot for semi-arid coastal
484 environments experiencing enhanced warming and intensified hydrological cycles. It is important to note that the specific
485 threshold of >45 mm identified here is characteristic of the climatological moisture capacity of the EM during extreme summer
486 anomalies. While the exact numerical value of this 'Critical Error Culmination' will vary geographically depending on local
487 atmospheric dynamics and latitude, the underlying physical principle remains universal: empirical T_m models systematically
488 degrade proportionally to the total atmospheric moisture mass during severe local extremes. The core vulnerability exposed in
489 this research—that static global models are structurally blind to sharp boundary layer thermodynamic decoupling during peak
490 insolation—is a fundamental physics problem, not a local anomaly. Therefore, the proposed synergistic MWR-GNSS retrieval
491 architecture provides a universally applicable solution for mitigating systematic dry biases in any complex terrain or coastal
492 environment globally.



493 Finally, our component-wise uncertainty analysis clarifies the error propagation chain in the GNSS-PWV conversion process,
494 shifting the paradigm of where optimization efforts should be focused. Historically, significant effort within the geodetic
495 community has been expended on refining atmospheric refractivity constants. However, we demonstrate that the error induced
496 by transitioning from the historical Davis et al. (1985) formulations to the modern Rüeiger (2002) constants is practically
497 negligible (<0.2 mm) for synoptic meteorological applications. The true "weak link" in the retrieval chain is unequivocally the
498 thermodynamic parameterization, which introduces errors an order of magnitude larger.

499

500 **5 Conclusion**

501 This study demonstrated that the accuracy of GNSS-derived Precipitable Water Vapor (PWV) in the Eastern Mediterranean
502 region, is fundamentally limited by the thermodynamic rigidity of static climatological models. By implementing a synergistic
503 retrieval strategy that couples GNSS delays with real-time ground-based microwave radiometry (MWR), we successfully
504 quantified and mitigated these limitations. The investigation yielded three primary methodological conclusions. First, we
505 established that standard empirical models (e.g., HGPT2) are structurally incapable of resolving the diurnal thermodynamic
506 decoupling between the boundary layer and free troposphere. This deficiency leads to severe systematic errors (the "noon
507 ballooning" effect) exceeding 6 K in weighted mean temperature (T_m) during peak solar insolation, which directly propagates
508 into a PWV bias >1.0 mm during extreme hygrometric events. Second, the MWR proved to be a superior source for
509 thermodynamic path delays, provided that site-specific calibration is applied. The development of a linear bias correction
510 scheme reduced the MWR T_m root-mean-square error from 2.32 K to 1.43 K. This correction effectively halves the uncertainty
511 in the final GNSS water vapor product compared to standard climatological approaches. Third, the sensitivity analysis
512 confirmed that thermodynamic input quality is the dominant error source in GNSS meteorology, outweighing uncertainties in
513 refractive index constants by an order of magnitude. Consequently, the proposed combined retrieval is not merely an
514 incremental improvement but a necessary architectural upgrade for monitoring severe weather.

515 For the climate-sensitive EM region, relying on static models for GNSS processing risks systematically masking moisture
516 trends during heatwaves and deep convection. We therefore recommend the operational integration of collocated MWR
517 observations into national GNSS processing chains. Where collocation is not feasible, future work should focus on assimilating
518 MWR-derived diurnal shape functions into static models to bridge the gap between climatology and reality. This study
519 establishes the "Corrected Synergistic Method" as a robust benchmark for generation of climate-quality water vapor datasets
520 in complex thermodynamic environments.

521



522 **Data availability**

523 The MWR and GNSS data used in this study are available from the CYGMEN project archive upon request. High resolution
524 Radiosonde data available from the Department of Meteorology (DoM), Cyprus. The ERA5 reanalysis data can be downloaded
525 from the Copernicus Climate Change Service (C3S) Climate Data Store.
526

527 **Author contributions**

528 ANP carried out the GNSS, MWR, and Radiosonde data processing, performed the synergistic PWV retrievals and error
529 diagnosis, and wrote the initial version of the paper. CO and HH conceptualized the study, acquired the funding and resources
530 for the CYGMEN infrastructure, and supervised the investigation. All authors discussed the results, edited, and proofread the
531 paper..
532

533 **Competing interests**

534 All authors declare that they have no conflict of interest.
535

536 **Acknowledgements**

537 We would like to express our sincere gratitude to the Cyprus Department of Meteorology (DoM) and in particular to Physicist
538 and Meteorology Officer Dr. Demetris Charalambous, for his invaluable guidance and for providing access to essential
539 resources at Athalassa observatory in Nicosia, Cyprus.
540

541 **Financial support**

542 The present study is funded by the Strategic Infrastructure project CYGMEN, which is implemented in the frames of Cohesion
543 Policy Programme “THALIA 2021-2027” and is co-funded by the European Union.
544

545 **References**

546 Askne, J. and Nordius, H.: Estimation of tropospheric delay for microwaves from surface weather data, Radio Sci., 22, 379–
547 386, <https://doi.org/10.1029/RS0221003p00379>, 1987.



- 548 Bennartz, R. and Bauer, P.: Sensitivity of microwave radiances at 85–183 GHz to precipitating ice particles, *Radio Sci.*, 38,
549 8075, <https://doi.org/10.1029/2002RS002626>, 2003.
- 550 Bennitt, G. V. and Jupp, A.: Operational assimilation of GPS zenith total delay observations into the Met Office numerical
551 weather prediction models, *Mon. Weather Rev.*, 140, 2706–2719, <https://doi.org/10.1175/MWR-D-11-00156.1>, 2012.
- 552 Bevis, M., Businger, S., Herring, T. A., Rocken, C., Anthes, R. A., and Ware, R. H.: GPS meteorology: Remote sensing of
553 atmospheric water vapor using the Global Positioning System, *J. Geophys. Res.*, 97, 15787–15801,
554 <https://doi.org/10.1029/92JD01517>, 1992.
- 555 Bevis, M., Businger, S., Chiswell, S., Herring, T. A., Anthes, R. A., Rocken, C., and Ware, R. H.: GPS meteorology: Mapping
556 zenith wet delays onto precipitable water, *J. Appl. Meteorol.*, 33, 379–386, [https://doi.org/10.1175/1520-0450\(1994\)033<0379:GMMZWD>2.0.CO;2](https://doi.org/10.1175/1520-0450(1994)033<0379:GMMZWD>2.0.CO;2), 1994.
- 558 Böhm, J., Möller, G., Schindelegger, M., Pain, G., and Weber, R.: Development of an improved empirical model for slant
559 delays in the troposphere (GPT2w), *GPS Solut.*, 19, 433–441, <https://doi.org/10.1007/s10291-014-0403-7>, 2015.
- 560 Bolton, D.: The computation of equivalent potential temperature, *Mon. Weather Rev.*, 108, 1046–1053, 1980.
- 561 Brenot, H., Neméghaire, J., Delobbe, L., Clerbaux, N., De Meutter, P., Deckmyn, A., Delcloo, A., Frappez, L., and Van
562 Roozendael, M.: Preliminary signs of the initiation of deep convection by GNSS, *Atmos. Chem. Phys.*, 13, 5425–5449,
563 <https://doi.org/10.5194/acp-13-5425-2013>, 2013.
- 564 Cimini, D., Westwater, E. R., Gasiewski, A. J., Klein, M., Leuski, V. Y., and Dowlatshahi, S.: Thermodynamic atmospheric
565 profiling during the 2010 Winter Olympics using ground-based microwave radiometry, *IEEE T. Geosci. Remote*, 49, 4959–
566 4969, <https://doi.org/10.1109/TGRS.2011.2154337>, 2011.
- 567 Crewell, S. and Lohnert, U.: Accuracy of boundary layer temperature profiles retrieved with multifrequency multiangle
568 microwave radiometry, *IEEE T. Geosci. Remote*, 45, 2195–2201, 2007.
- 569 Douša, J. and Václavovic, P.: Real-time zenith tropospheric delays in support of numerical weather prediction applications,
570 *Adv. Space Res.*, 53, 1347–1358, <https://doi.org/10.1016/j.asr.2014.02.021>, 2014.
- 571 Davis, J. L., Herring, T. A., Shapiro, I. I., Rogers, A. E. E., and Elgered, G.: Geodesy by radio interferometry: Effects of
572 atmospheric modeling errors on estimates of baseline length, *Radio Sci.*, 20, 1593–1607,
573 <https://doi.org/10.1029/RS020i006p01593>, 1985.



- 574 Gaffen, D. J.: Temporal inhomogeneities in radiosonde temperature records, *J. Geophys. Res.*, 99, 3667–3676,
575 <https://doi.org/10.1029/93JD03179>, 1994.
- 576 Giannadaki, D., Oikonomou, C., Haralambous, H., Tymvios, F., and Loizou, E.: Validation of precipitable water vapour
577 products using CyMETEO GNSS network in Cyprus, in: Eleventh International Conference on Remote Sensing and
578 Geoinformation of the Environment (RSCy2025), Vol. 13816, 397–409, SPIE, 2025.
- 579 Giorgi, F.: Climate change hot-spots, *Geophys. Res. Lett.*, 33, L08707, <https://doi.org/10.1029/2006GL025734>, 2006
- 580 Guerova, G., Jones, J., Douša, J., Dick, G., de Haan, S., Pottiaux, E., Bock, O., Pacione, R., Elgered, G., Vedel, H., and Bender,
581 M.: Review of the state of the art and future prospects of the ground-based GNSS meteorology in Europe, *Atmos. Meas. Tech.*,
582 9, 5385–5406, <https://doi.org/10.5194/amt-9-5385-2016>, 2016.
- 583 Held, I. M. and Soden, B. J.: Robust responses of the hydrological cycle to global warming, *J. Climate*, 19, 5686–5699,
584 <https://doi.org/10.1175/JCLI3990.1>, 2006.
- 585 Jiang, P., Ye, S., Chen, D., Liu, Y., and Xia, P.: Development of time-varying global gridded Ts-Tm model for precise GPS-
586 PWV retrieval, *Atmos. Meas. Tech.*, 12, 1233–1249, <https://doi.org/10.5194/amt-12-1233-2019>, 2019.
- 587 Jones, J., Guerova, G., Douša, J., Dick, G., de Haan, S., Pottiaux, E., Bock, O., Pacione, R., Elgered, G., Vedel, H., and Bender,
588 M.: *Advanced GNSS Tropospheric Products for Monitoring Severe Weather Events and Climate*, Springer, Cham,
589 <https://doi.org/10.1007/978-3-030-28909-6>, 2020.
- 590 Kiehl, J. T. and Trenberth, K. E.: Earth's annual global mean energy budget, *B. Am. Meteorol. Soc.*, 78, 197–208,
591 [https://doi.org/10.1175/1520-0477\(1997\)078<0197:EAGMEB>2.0.CO;2](https://doi.org/10.1175/1520-0477(1997)078<0197:EAGMEB>2.0.CO;2), 1997.
- 592 Lan, Z., Zhang, B., and Geng, T.: Establishment and analysis of global gridded Tm-Ts relationship model, *Geodesy and*
593 *Geodynamics*, 7, 101–107, <https://doi.org/10.1016/j.geog.2016.02.001>, 2016.
- 594 Lelieveld, J., Hadjinicolaou, P., Kostopoulou, E., Chenoweth, J., El Maayar, M., Giannakopoulos, C., Hannides, C., Lange,
595 M. A., Tanarhte, M., Tyrlis, E., and Xoplaki, E.: Climate change and impacts in the Eastern Mediterranean and the Middle
596 East, *Climatic Change*, 114, 667–687, <https://doi.org/10.1007/s10584-012-0418-4>, 2012.
- 597 Li, H., Wang, X., Wu, S., Zhang, K., Chen, X., Qiu, C., Zhang, Q., and Li, L.: Development of an improved model for
598 prediction of short-term heavy precipitation based on GNSS-derived PWV, *Remote Sens.*, 12, 4101,
599 <https://doi.org/10.3390/rs12244101>, 2020.



- 600 Löhnert, U. and Maier, O.: Operational profiling of temperature using ground-based microwave radiometry at Payerne:
601 Prospects and challenges, *Atmos. Meas. Tech.*, 5, 1121–1134, <https://doi.org/10.5194/amt-5-1121-2012>, 2012.
- 602 Mateus, P., Mendes, V. B., and Plecha, S. M.: HGPT2: an ERA5-based global model to estimate relative humidity, *Remote*
603 *Sens.*, 13, 2179, <https://doi.org/10.3390/rs13112179>, 2021.
- 604 Ning, T. and Elgered, G.: Intercomparison of MAX-DOAS vertical profile retrieval algorithms: studies on field data from the
605 CINDI-2 campaign, *Atmos. Meas. Tech.*, 14, 1–35, <https://doi.org/10.5194/amt-14-1-2021>, 2021.
- 606 Pakkattil, A., Parde, A. N., Wagh, S., Lonkar, P., and Ghude, S. D.: Wintertime Intercomparison of Specific Humidity and
607 Temperature Profiles Measured by Microwave Radiometer (MWR), Radiosonde, and INSAT-3DR Sounder Over Delhi, India,
608 *J. Geophys. Res. Atmos.*, 130, e2025JD044462, <https://doi.org/10.1029/2025JD044462>, 2025.
- 609 Parde, A. N., Ghude, S. D., Prasad, V. S., Hari Prasad, K. B. R. R., Dhangar, N. G., Lonkar, P., and Rajeevan, M.: Influence
610 of ground-based microwave radiometer profile assimilation on fog genesis forecasts in the winter boundary layer of Northern
611 India, *J. Geophys. Res. Atmos.*, 130, e2024JD042224, <https://doi.org/10.1029/2024JD042224>, 2025.
- 612 Oikonomou, C., Tymvios, F., Pikridas, C., Bitharis, S., Balidakis, K., Michaelides, S., ... and Charalambous, D.: Tropospheric
613 delay performance for GNSS integrated water vapor estimation by using GPT2w model, ECMWF's IFS operational model and
614 in situ meteorological data, *Adv. Geosci.*, 45, 363–375, <https://doi.org/10.5194/adgeo-45-363-2018>, 2018.
- 615 Realini, E., Gatti, A., Reguzzoni, M., Sampietro, D., and Venuti, G.: GNSS-based precipitable water vapor retrieval for severe
616 weather monitoring: The 2014 Genoa flood case study, *Adv. Space Res.*, 53, 1–10, <https://doi.org/10.1016/j.asr.2014.02.015>,
617 2014.
- 618 Rüeger, J. M.: Refractive index formulae for radio waves, in: Proceedings of the FIG XXII International Congress,
619 Washington, D.C., USA, 19–26 April 2002, 1–13, 2002.
- 620 Ross, R. J. and Elliott, W. P.: Tropospheric water vapor climatology and trends over North America: 1973–93, *J. Climate*, 9,
621 3561–3574, 1996.
- 622 Saastamoinen, J.: Atmospheric correction for the troposphere and stratosphere in radio ranging satellites, in: The Use of
623 Artificial Satellites for Geodesy, *Geophys. Monogr. Ser.*, 15, 247–251, AGU, Washington, D.C.,
624 <https://doi.org/10.1029/GM015p0247>, 1972.
- 625 Soden, B. J. and Lanzante, J. R.: An assessment of satellite and radiosonde climatologies of upper-tropospheric water vapor,
626 *J. Climate*, 9, 1235–1250, [https://doi.org/10.1175/1520-0442\(1996\)009<1235:AAOSAR>2.0.CO;2](https://doi.org/10.1175/1520-0442(1996)009<1235:AAOSAR>2.0.CO;2), 1996.



- 627 Steinke, S., Ebell, K., Löhnert, U., Bozzo, A., Crewell, S., and Turner, D. D.: Assessment of small-scale integrated water
628 vapour variability during HOPE, *Atmos. Chem. Phys.*, 15, 2675–2692, <https://doi.org/10.5194/acp-15-2675-2015>, 2015.
- 629 Thayer, G. D.: An improved equation for the radio refractive index of air, *Radio Sci.*, 9, 803–807,
630 <https://doi.org/10.1029/RS009i010p00803>, 1974.
- 631 Trenberth, K. E., Fasullo, J., and Smith, L.: Trends and variability in column-integrated atmospheric water vapor, *Clim.*
632 *Dynam.*, 24, 741–758, <https://doi.org/10.1007/s00382-005-0017-4>, 2005.
- 633 Tomasi, C.: Vertical distribution features of atmospheric water vapor in the Mediterranean, Red Sea, and Indian Ocean, *J.*
634 *Geophys. Res.*, 89, 2563–2566, <https://doi.org/10.1029/JD089iD02p02563>, 1984.
- 635 Van Malderen, R., Brenot, H., Pottiaux, E., Beirle, S., Hermans, C., De Mazière, M., ... and Bruyninx, C.: A multi-site
636 intercomparison of integrated water vapour observations for climate change analysis, *Atmos. Meas. Tech.*, 7, 2487–2512,
637 <https://doi.org/10.5194/amt-7-2487-2014>, 2014.
- 638 Van Malderen, R., Pottiaux, E., Klos, A., Domonkos, P., Elias, M., Ning, T., ... and Bock, O.: Homogenizing GPS precipitable
639 water vapor time series: Benchmarking homogenization algorithms on synthetic datasets, *Remote Sens.*, 14, 1050,
640 <https://doi.org/10.3390/rs14041050>, 2022.
- 641 Vaquero-Martínez, J., Antón, M., Ortiz de Galisteo, J. P., Cachorro, V. E., Wang, H., González-Abad, G., ... and Costa, M. J.:
642 Inter-comparison of integrated water vapor from ground-based GPS and satellite remote sensing at Mediterranean sites, *IEEE*
643 *J. Sel. Top. Appl.*, 11, 1718–1728, <https://doi.org/10.1109/JSTARS.2018.2812804>, 2018.
- 644 Weaver, C. P. and Ramanathan, V.: Deductions from a simple climate model: Factors governing surface temperature and
645 atmospheric thermal structure, *J. Geophys. Res.*, 100, 11585–11591, <https://doi.org/10.1029/95JD00774>, 1995.
- 646 Yao, Y., Zhang, B., Yue, S., Xu, C., and Peng, W.: Analysis of the global Tm-Ts correlation and establishment of the latitude-
647 related linear model, *Chin. Sci. Bull.*, 59, 2340–2347, <https://doi.org/10.1007/s11434-014-0275-9>, 2014.
- 648 Ziskin Ziv, S., Yair, Y., Alpert, P., Uzan, L., and Reuveni, Y.: The diurnal variability of precipitable water vapor derived from
649 GPS tropospheric path delays over the Eastern Mediterranean, *Atmos. Res.*, 249, 105307,
650 <https://doi.org/10.1016/j.atmosres.2020.105307>, 2021.
- 651 Ziskin Ziv, S., Alpert, P., and Reuveni, Y.: Long-term variability and trends of precipitable water vapour derived from GPS
652 tropospheric path delays over the Eastern Mediterranean, *Int. J. Climatol.*, 41, 6433–6454, <https://doi.org/10.1002/joc.7205>,
653 2021.

<https://doi.org/10.5194/egusphere-2026-231>

Preprint. Discussion started: 3 March 2026

© Author(s) 2026. CC BY 4.0 License.



654 Zittis, G., Hadjinicolaou, P., Klangidou, M., et al.: A multi-model, multi-scenario, and multi-domain analysis of regional
655 climate projections for the Mediterranean, *Reg. Environ. Change*, 19, 2621–2635, <https://doi.org/10.1007/s10113-019-01565->
656 w, 2019.